Evaluating the impact of a time-evolving constellation on multi-platform satellite based daily precipitation estimates

Rômulo Augusto Jucá Oliveira, Rémy Roca, Stephan Finkensieper, Sophie Cloché, Marc Schröder

Atmospheric Research 279 (2022) 106414

Contents lists available at ScienceDirect

Atmospheric Research

journal homepage: www.elsevier.com/locate/atmosres

Evaluating the impact of a time-evolving constellation on multi-platform satellite based daily precipitation estimates

Rômulo Augusto Jucá Oliveira [a], Rémy Roca [a,*], Stephan Finkensieper [b], Sophie Cloché [c], Marc Schröder [b]

[a] Laboratoire d'Études en Géophysique et Océanographie Spatiales (Université de Toulouse III, CNRS, CNES, IRD), Toulouse, France
[b] Deutscher Wetterdienst, Offenbach, Germany
[c] IPSL, Palaiseau, France

ARTICLE INFO

Keywords:
Satellite precipitation
Uncertainty
Microwave constellation

ABSTRACT

Satellite based precipitation climate data records (CDRs) have recently emerged and provide new observational sources to characterize of the changing nature of global precipitation. These products rely on the use of passive microwave instruments. At the daily scale, these CDRs are prone to performance sensitivity resulting from the availability of microwave observations. As the configuration of the microwave sounders and imagers fleet evolves over time, adding new satellites and instruments or losing old platforms, the climate-oriented performances of the CDRs are likely impacted. In this study, this effect is quantified using a prototype constellation-based quasi-global precipitation product algorithm and data-denial experiments. The constellation change has a small impact of the long-term average climatology both in terms of mean and distribution recalling the resilience of the climatology of such a multi-platform product to the fluctuations of the amount of available input data. The interannual variability on the other hand is more impacted. More large rainfall amounts are relatively more perturbed than the lower rain daily accumulation with anomalies up to 30% for some configurations. The method to correct for the artefact is detailed and while some aspects of the computations are product-specific, the major outcome of this study should apply to various similar products as well.

1. Introduction

Water and energy cycles are central to the physics of climate change (Stephens et al., 2020). Precipitation is at the heart of these cycles and the physical drivers of the change in the precipitation distribution are being investigated mainly thanks to modelling efforts (Chen et al., 2019; Pendergrass and Hartmann, 2014a) as observational constraints are limited (Contractor et al., 2021). Indeed, owing to large natural variability and scarce conventional networks, the observation based documentation of its recent evolution with global warming has remained notoriously difficult to achieve (Morin, 2011). A suite of satellite-based products has emerged over the past decades offering new insights in the recent climate evolution of the water cycle (Levizzani and Cattani, 2019). While most of these products were not designed for climate applications (Levizzani et al., 2018), there is now a large number of precipitation datasets spanning >20 years, even at the daily scale (Roca et al., 2019). These emerging climate data records (CDRs) are making use of a variety of satellite observations, ranging from infrared geostationary based radiances up to the passive microwave imagers and sounders data from various platforms.

The products ingesting microwave data have been shown to outperform the other products on various climatological metrics (Beck et al., 2017; Sun et al., 2018; Maggioni et al., 2016). Over land, satellite precipitation products that are calibrated against rain-gauge data overall show good performance compared to gridded in-situ datasets in monitoring extreme precipitation, and perform better than reanalysis based products (Bador et al., 2020; Alexander et al., 2020). The no-gauges satellite products do show overall poorer performance with respect to their calibrated counterparts. Yet, Liu and Allan (2012) showed that some earlier versions of the CDRs exhibit stability issues over the length of the record. This is confirmed at daily scale and for the most recent versions of the CDRs and further limitations for the representation of extreme precipitation is identified (Masunaga et al., 2019). Investigation of the interannual variability in the daily precipitation

* Corresponding author at: Observatoire Midi-Pyrénées, Laboratoire d'Etudes Géophysiques et d'Océanographie Spatiales, 14 Avenue Edouard Belin, 31400 Toulouse, France.
E-mail address: remy.roca@legos.obs-mip.fr (R. Roca).

https://doi.org/10.1016/j.atmosres.2022.106414
Received 10 May 2022; Received in revised form 22 August 2022; Accepted 22 August 2022
Available online 26 August 2022

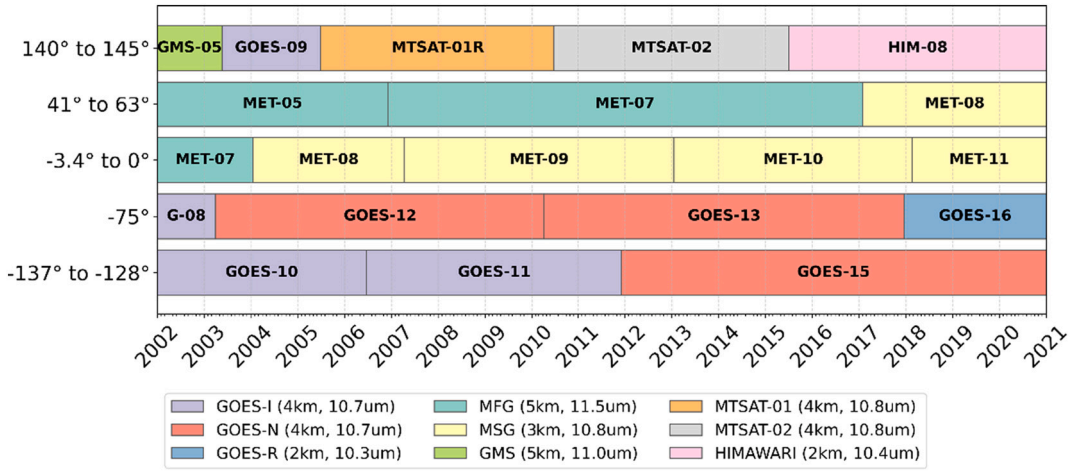

Fig. 1. Overview of the available geostationary platform from 2002 to 2019. Colors indicate the platform series. Acronyms: MFG = Meteosat First Generation, MSG = Meteosat Second Generation.

distribution also revealed significant departure between the GPCP and TRMM 3B42v7 products in the Tropics (Pendergrass and Hartmann, 2014b). While a number of studies help to document the limitations and issues in the satellite data based products, owing to the complexities of these Level-4 products, it remains difficult to relate these limitations to the algorithm's underlying assumptions and/or data (Roca et al., 2021).

Indeed, microwave based-precipitation CDR can use a single or multiple platform all throughout their record. The Global Precipitation Climatology Project (GPCP) for instance, relies on the use of a single platform, the 6 PM local equator crossing time microwave imager (Huffman et al., 2001). Abrupt breaks in the time series can occur when changes of the instruments take place, like the replacement of SSM/I by SSMI/S (Adler et al., 2018; Potter et al., 2020). The use of multiple platforms, collectively known, as the Global Precipitation Measurement (GPM) microwave constellation for precipitation estimates benefit from the inputs from many platforms and has been shown to improve the overall performance of the product thanks to enhanced sampling (Roca et al., 2018; Joyce et al., 2004; Huffman et al., 2018). Yet, the methodology to merge these various sources of data is often complex and as a consequence, the performances of these new products are sensitive to the number of microwave platforms available in a product-specific way (Joyce et al., 2004; Ayat et al., 2021; Rajagopal et al., 2021). Chambon et al. (2013a) have shown that the configuration of the constellation, i.e., the number of microwave imagers in a constellation, can indeed significantly alter daily precipitation estimation in the Tropical Amount of Precipitation with an Estimate of ERrors (TAPEER) framework (Chambon et al., 2012).

As the configuration of the constellation changes over time, these kind of performance issues propagate upscale and the multi-platforms CDRs are not free from climate-relevant issues. The constellation configuration indeed evolves in time and can be composed of as low as a single platform up to >12 (Kidd et al., 2021a). As a consequence, any precipitation CDR relying on microwave data is expected to reveal some sensitivity to the time-dependent constellation configuration. In this study, we propose to quantify such an artefact using a full-fledged precipitation estimate algorithm and data-denial experiments. We also propose a way to statistically account for these modifications of the constellation on the daily precipitation distribution monitoring.

The estimation algorithm and the satellite data are first introduced along with ground-based evaluation datasets. Then the data-denial methodology is presented together with the variations in time of the constellation. Results are summarized in Section 4 and a conclusion ends the paper.

2. Data

2.1. The 2006–2019 GIRAFE record

2.1.1. The GIRAFE algorithm

The Global Interpolated RAinFall Estimation (GIRAFE) is a 1°/daily precipitation product developed for monitoring the climate globally, ultimately covering the period from 2000 onwards (Roca et al., 2020) and is implemented and operated by the European Organization for the Exploitation of Meteorological Satellites (EUMETSAT) Satellite Application Facility on Climate Monitoring (CM SAF). GIRAFE evolves from the TAPEER approach (Roca et al., 2018), which is based on the Universally Adjusted GOES Precipitation Index (UAGPI) technique (Xu et al., 1999; Kidd et al., 2003). Therefore, the 1°/daily rain accumulation (R_{ACC}, in mm day^{-1}) is computed using the passive microwave constellation (sounders and imagers) conditional rain rates (R_{COND}, in mm h^{-1} – the intensity parameter) and the fraction of precipitating clouds ($R_{FRAC,}$ in % - the detection information) from geostationary infrared imagery observations up to 55° N/S. Poleward of this, only the passive microwave observations are used. In this study, we restrict the analysis to the 55° N/S region where both microwave and IR data are merged together. The observing system (the constellation of PMW and geostationary satellites) used behind the GIRAFE algorithm for computing the 1°/daily precipitation are detailed in next sections. Only the period 2006–2019 is currently used as some earlier geostationary observations requires further quality control and will be implemented in the operational product in the near future.

2.1.2. The GPROF and PRPS Level-2 products

GIRAFE also retains the flexible feature of TAPEER regarding the use of more instantaneous rain rate retrievals from Level-2 (L2) PMW algorithms. For the imagers and most of the sounders, the GPROF2017 for GPM V05 database data are used (Kummerow et al., 2015). This recent version of GPROF benefited from several improvements (e.g., on the physical approaches, the cloud and rain profile a-priori databases, the determination of a precipitation detection threshold, among others) compared to the original version (Kummerow et al., 1996). In order to also benefit from the dense tropical sampling of the Megha-Tropiques mission (Roca et al., 2015), PRPS L2 using SAPHIR is used (Kidd et al., 2021b). We use the most recent PRPS algorithm and database version (PRPS2019 for GPM V06 database). The PRPS-SAPHIR rain retrievals are computed based on the relation between the near surface rain rate from the GPM Dual frequency Precipitation Radar (DPR) and the brightness temperature (TB) radiances from SAPHIR held in an a-priori database. Both the GPROF and PRPS L2 PMW retrievals are

available in the "real time" (L2) and climate (2A-CLIM) database versions. The differences between the L2 and 2A-CLIM lies in the ancillary products used in the initial processing step that associates the model's parameters with the TBs database observations. The 2A-CLIM products make use of the JMA's Global ANALysis (GANAL) and the 2A-CLIM products utilize ECMWF ERA- Interim database. We opted for considering the 2A-CLIM product version in view of its long-term availability, which makes it possible to access certain platforms (e.g., TMI) that are not available in the other database. The GPROF and PRPS data were obtained from the NASA Precipitation Processing System (PPS) data-access platform.

GPROF is a well-documented product and is used in GIRAFE as a reference for the L2 inputs. Yet GPROF is not free from limitations. In general, GPROF indeed tends to overestimate (underestimate) the light (heavy) rainfall amounts. The underestimation of heavy precipitation volumes by GPROF retrieval algorithm is a known artefact of Bayesian approach that averages multiple profiles, which consequently gives less weight to most extreme precipitation intensities in the database (You et al., 2020). However, over Central Amazon, overestimation of rain occurrences can be linked to the ice scattering signals from convective clouds (high ice water path contents), which are not always consistently related to the surface precipitation (Costa et al., 2018).

2.1.3. The GEOring archive

The ring of geostationary meteorological satellites consists in a fleet of geostationary satellites located at the specific location along the Equator, each providing whole-disk imagery of the Earth, hereafter referred to as the GEOring. The GEOring configuration has been evolving since 2002 as shown in Fig. 1. Infrared observations from the GEOring are used in GIRAFE. Indeed, all sensors feature a ~ 10.5-μm IR channel with a spatial resolution ranging from 2 to 5 km at nadir. The temporal sampling ranges from 10 to 30 min, including partial scans of the Northern and Southern Hemisphere. Level 1 datasets for the entire time series have been collected from the corresponding agencies (EUMETSAT, NOAA, JMA/JAXA). The open source Python library Satpy (Raspaud et al., 2021) is used to read the various binary data formats and calibrate raw image counts to brightness temperatures. The GIRAFE algorithm does not require intercalibration of geostationary imagers (Roca et al., 2020) but resampling to the final grid (partial scans to full disk; oversampled to uniformly sampled) and quality control is performed. Given the particular characteristics of each platform, all the geostationary satellite datasets that comprise the five different regions, are processed and quality-controlled independently (Fiolleau et al., 2020). Images from older sensors, in particular, can have various defects that affect the quality of the derived rain estimates. Therefore, it is important to identify and exclude these images. For this purpose, an automatic quality control algorithm is independently applied to the entire IR archive (Szantai et al., 2011).

2.1.4. Implementation aspects

The implementation of the GIRAFE algorithm requires a definition of a training data set to determine R_{cond} and another one to determine the rain-no rain IR threshold (Roca et al., 2020) which can influence the performance of the product (Roca et al., 2018). Here the same training data set is used for the two steps and is set to 5°x5°x5 days in order to accommodate the earlier part of the record with a less populated constellation than for the recent epoch. Following a sensitivity study of the GPROF product, a threshold of 0.5 mm h^{-1} is used for detection. The computation of R_{cond} is performed using a larger threshold of 1.5 mm h^{-1} to avoid the estimate to be biased low because of light rains, especially over the ocean (Roca et al., 2018). The framework training volume of 5° x 5° x 5 days was adopted for both the intensity and detection parameters.

2.2. Ground based data for validation

In order to assess the suite of data-denial experiments from the multiple constellation configurations' periods carried out during two different seasons: June–July-August (JJA) of 2014 and December–January-February (DJF) of 2014/5, for two tropical regions West Africa and Brazil, respectively. Over both regions, a consolidated daily accumulated precipitation database of several gauged-networks is available. Over West Africa, during the monsoon, Niger experiences precipitation from both local convection and organized convective systems. Therefore, the assessments are focused on the AMMA-CATCH observatory (AMMA-CATCH, 1990); specifically over the 1° Niger site (AMMA-CATCH Niger, 1990). The 1°x1°/daily rainfall amount is estimated from this high-quality rain-gauges thanks to block-kriging. This dataset has been considered as a reference by several studies under the assessments of satellite precipitation estimates (e.g., Roca et al., 2010; Kirstetter et al., 2013; Gosset et al., 2018).

Over Brazil, the analyses were carried out for the whole country during the period of DJF of 2014/5 - the rainy season in much of Brazil. A daily gridded precipitation database (at 1°/daily of spatial/temporal resolution), is composed of several daily accumulated precipitation observations distributed over the country and are considered as ground reference for the data-denial experiments' assessments. The daily gauged-precipitation observations, recorded from 12 to 12 UTC, used for composing the gridded precipitation fields, were obtained from multiple agencies, primarily from the Centre for Weather Forecasting and Climatic Studies [Centro de Previsão de Tempo e Estudos Climáticos (CPTEC)] of the Brazilian National Institute for Space Research [Instituto Nacional de Pesquisas Espaciais (INPE)] and from HYdrogeochemistry of the AMazonian Basin (HYBAM), which are responsible to collect and apply a primary quality control (QC). The rain gauges are operated by multiple federal and regional institutions, such as the Brazilian National Water and Sanitation Agency [Agência Nacional de Águas e Saneamento Básico (ANA) in Portuguese], Brazilian National Institute of Meteorology [Instituto Nacional de Meteorologia (INMET)], Foundation Cearense for Meteorology and Water Management [Fundação Cearense de Meteorologia e Recursos Hídricos (FUNCEME)] and other regional agencies. In this study, grid cells of 1°/daily resolution with 100% temporal coverage and containing at least 5 rain gauges are considered for the period under investigation.

It is worth mentioning that one of the main characteristics of the DJF climatology over Brazil, is the remarkable spatial variability of precipitation due to both the occurrence and intensity of precipitation, which are a consequence of multiple atmospheric mechanisms that drive the South American monsoon system (SAMS) life cycle (Raia and Cavalcanti, 2008; Marengo et al., 2012). Given that, the contribution of distinct precipitating systems acting from local to synoptic scales, as well as the influence of remote forcing, i.e., the El Niño–Southern Oscillation (ENSO), can distinctly impact and modulate the quality of rainy-season distribution across the country (Reboita et al., 2010; Cai et al., 2020). For instance, the DJF 2014/5 rainy season experienced the influence of large-scale weather conditions that produced negative anomalies over the southeast of Brazil (Coelho et al., 2016). Over the Central Amazon, in addition to meso- and large-scale factors, several local influences play an important role modulating the rainfall occurrences, which affected the onset and end of the DJF 2014/5 rainy season in Central Amazon (Marengo et al., 2017) (Biscaro et al., 2021).

2.3. Preliminary assessment of GIRAFE/GPROF

The current implementation of the GIRAFE product is a prototype product that will evolve with the use of a reprocessed set of L2 rain-rate estimations in the future. The current GIRAFE product is a microwave and IR only product and does not include any adjustments of the GPROF dataset using radar observations. Similarly, unlike most of the daily gridded satellite products (Roca et al., 2019), no calibration against rain-

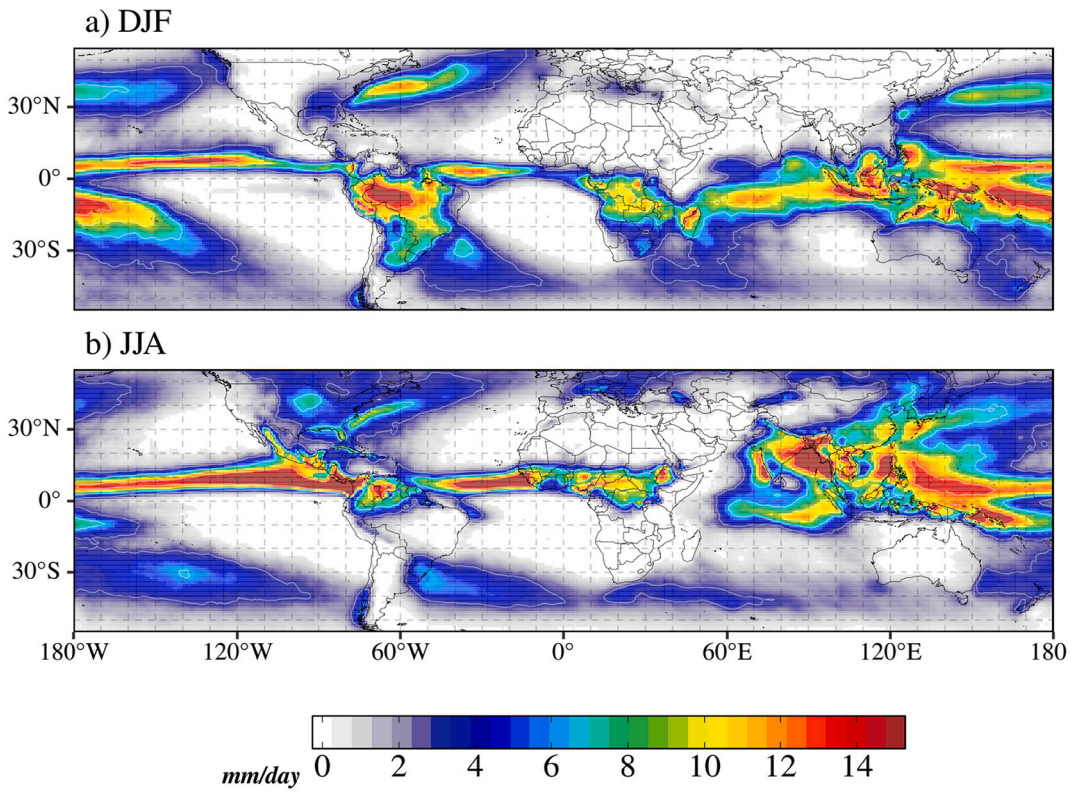

Fig. 2. The multi-year average (2006–2019) daily precipitation amount (in mm day^{-1}) for the Boreal a) Winter (December–January-February) and b) Summer (June–July-August) between 55°N/S, from GIRAFE product.

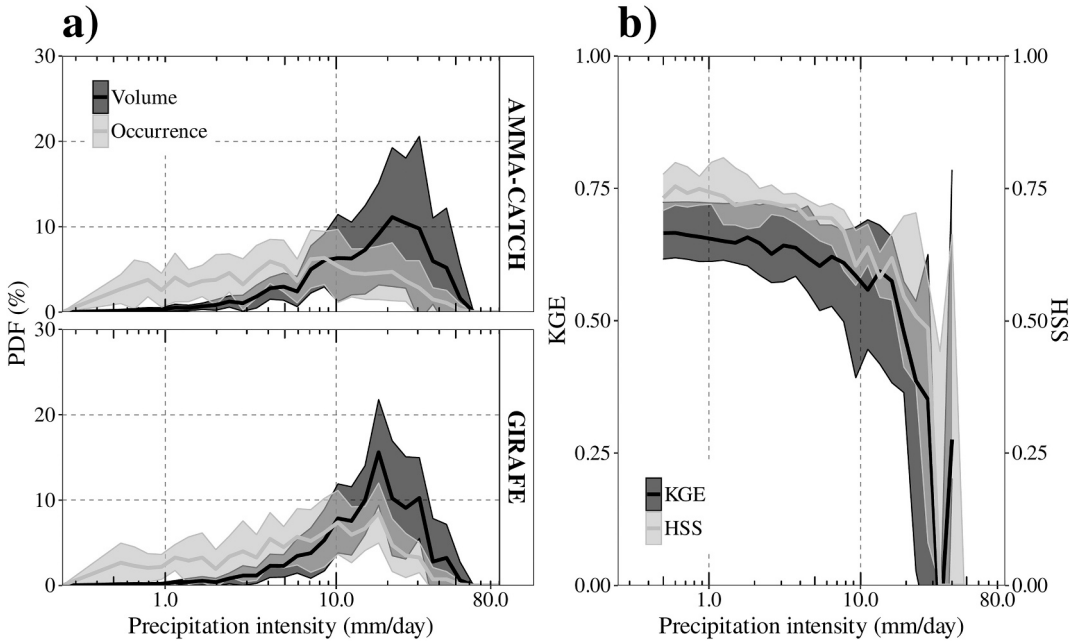

Fig. 3. Comparative analysis of the daily precipitation amounts (dark gray) and occurrences (light gray) between the GIRAFE product and the ground-based observations (AMMA-CATCH gridded data) over Niger site from 2006 to 2019: a) Probability density functions of precipitation volume and occurrence for the ground-based observations (upper-panel) and the GIRAFE (bottom-panel); and b) Continuous (KGE) and categorical (HSS) verification statistics as a function of the precipitation. Lines (shaded areas) represent the medians (standard deviation) multi-year distributions. Note that the x-axis is in the log-scale.

gauges is performed. As a consequence, such an experimental product is likely to well reflect the L2 related uncertainty. We provide a preliminary assessment of the protype product below. The conditional mean rainfall for the quasi-global land masses over the 2006–2019 period averages to 8.9 mm day^{-1} and to 15 mm day^{-1} for the oceanic regions.

Fig. 2 presents the Boreal Summer and Winter averages of the product that reveals the well-known features of the precipitation

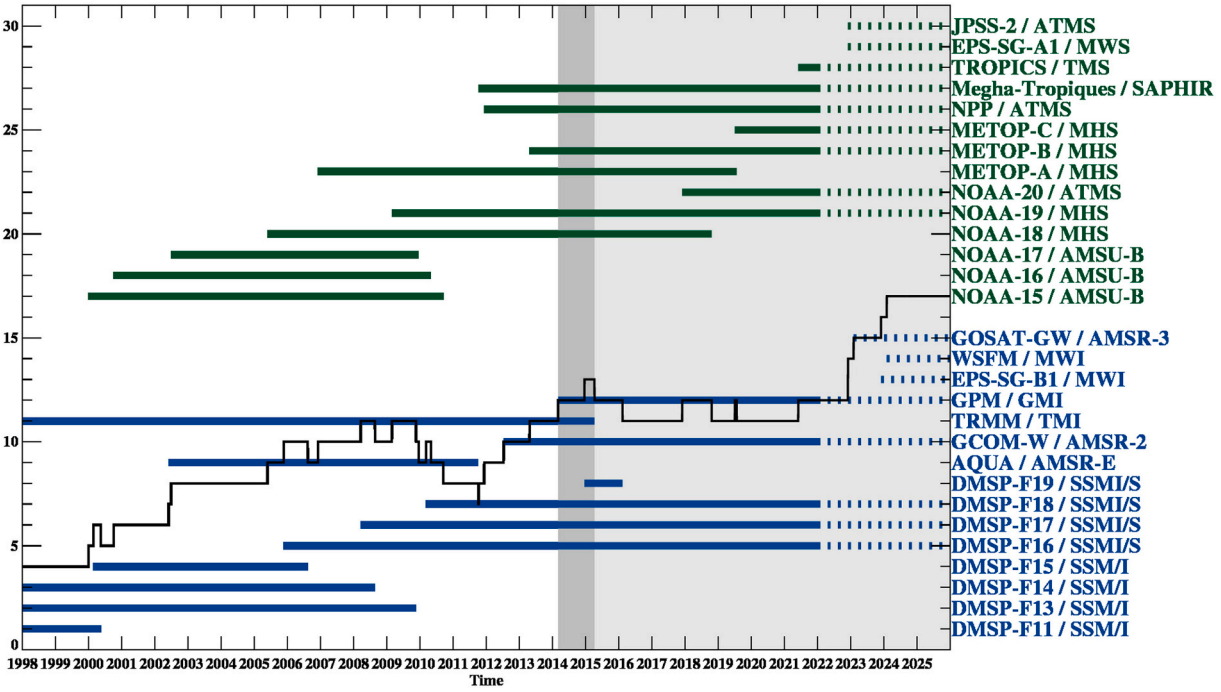

Fig. 4. Availability of PMW satellites showing the time-evolution of the constellation configuration of sounders (green) and imagers (blue) from 1998 to 2021 (solid lines) and the projected future mission up to 2025 (dashed lines). Solid black line is the total number of platforms. Shaded areas in dark and light gray correspond to the TRMM-to-GPM era transition and the GPM era periods, respectively. The data source is based upon the World Meteorological Office (WMO) Observing Systems Capability Analysis and Review Tool (OSCAR) database and the National Aeronautics and Space Administration (NASA) Precipitation Processing System (PPS) data archive for the Global Precipitation Measurement (GPM) mission. (For interpretation of the references to colour in this figure legend, the reader is referred to the web version of this article.)

distribution. One can also note a smooth continuity between the ocean and the land masses.

While the large-scale features are well represented and most of the distribution is well characterized, the current product suffers from difficulties in the representation of the large accumulation. Comparison with the Niger site ground observations highlights the weaker performance of the product for rain accumulation above 20 mm day^{-1} where KGE and HSS scores drop significantly compared to accumulation below 20 mm day^{-1} where the product performance is good (Fig. 3).

This limitation of the experimental product is mainly rooted in the characteristics of the GPROF retrievals. Comparison with ground based radar indeed revealed that the uncertainties over the Central Amazon and West Africa regions are also linked to the precipitation regime, system structure, and degree of organization: the rainfall overestimation can be attributed to deep-organized regimes while the underestimation is related to shallow and deep-unorganized regimes (Petković and Kummerow, 2017). Performance characteristics of GPROF can be also attributed to the substantial overestimation of the magnitude of the condensed water content profiles of the stratiform precipitation (Utsumi et al., 2020). Such performance characteristics are regardless of the surface type, despite less pronounced over land (i.e., vegetation) than over ocean surfaces – in-land water, coastal and semiarid regions also pose particular issues that lead to systematic increases in the false alarms (Oliveira et al., 2016; Tan et al., 2018). It is important to note that GPROF data are generally used to support higher level products for which, various adjustments (to radar-radiometer products and/or to rain-gauges) are performed (e.g., Huffman et al., 2018), partly mitigating these limitations. In short, the highlighted deficiencies of the experimental product are not detrimental to the sensitivity study and the data denial experiments, although the weaker performances of the product for high accumulation should be kept in mind when interpreting the results.

3. Method

3.1. Rationale and data denial experiments set-up

The rationale for our estimation of the sensitivity of the precipitation estimation to the configuration of the constellation consists in identifying a reference period for which the constellation is characterized by a maximum number of platforms. The precipitation estimation for that same period is done using various configurations where the baseline configuration is altered, through to data denial experiments. The two estimates are then compared to assess the sensitivity of the precipitation estimation to the configuration of the constellation. In this sense, our evaluation of the uncertainty associated to the changes of the configuration of the constellation is relative to the reference period.

The various configurations and the reference period are identified from the historical record to represent the evolution of the configuration over the last two decades (Fig. 4). We have here opted to pick the reference as the period that, over the few last decades, had the most contemporaneous operational platforms to emphasize the sensitivity to the number of sounders and imagers platforms in the configuration of the constellation. This focus was decided after evaluating the impact of the individual instrument performances or resolution changes, guided by previous results (Roca et al., 2018). Our data denial experiments are indeed limited to the inclusion or rejection of a full platform as to mimic the various configurations encountered over the past. Yet, the details of the Equator crossing times are not accounted for in these experiments but comparisons over land and ocean, show this to have a small impact. The current implementation hence tends provide the upper bound of the associated uncertainty. As shown below the small magnitude of such an upper bound of the uncertainty suggests a strong resilience of the GIRAFE approach to the configuration of the constellation. The comparisons between the experiments and the references are performed by pooling all the data by rain accumulation and the three-month long

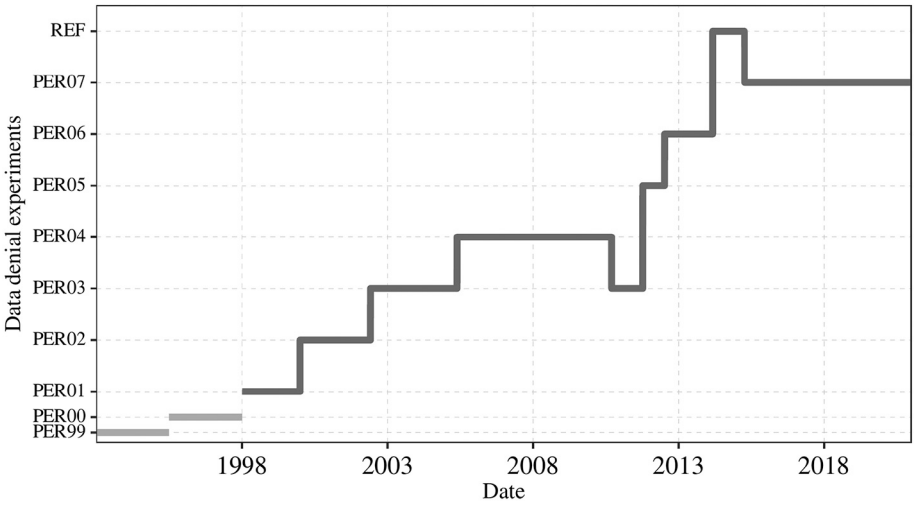

Fig. 5. Periods correspondent to the constellation configurations under consideration for the data denial experiments. Note that the Reference period (REF) is placed during the TRMM-to-GPM era transition (2014–2015), the so-called golden-era period. See text for details.

Table 1
Data denial experiments and their respective constellation configurations based on its correspondent period of satellite availabilities since 1998. The experiments were carried out globally (55° N/S), during JJA of 2014 and DJF of 2014/5.

Experiment	Period	Number of Platforms		Platforms from the reference period
		Imagers	Sounders	
REF	2014-03-04–2015-04-08	6	6	SSMI/S (3), GCOMW1, TMI, GMI, SAPHIR, MHS (4), ATMS
PER07	2015-04-09–2020-12-31	5	6	SSMI/S (3), GCOMW1, GMI, SAPHIR, MHS (4), ATMS
PER06	2012-07-10–2014-03-03	5	5	SSMI/S (3), GCOMW1, TMI, SAPHIR, MHS (3), ATMS
PER05	2011-10-11–2012-07-09	4	5	SSMI/S (3), TMI, SAPHIR, MHS (3), ATMS
PER04	2005-05-25–2010-09-15	5	5	SSMI/S (3), GCOMW1, TMI, MHS (4), ATMS
PER03	2002-06-01–2005-05-24 2010-09-16–2011-10-10	5	3	SSMI/S (3), GCOMW1, TMI, MHS (3)
PER02	2000-01-01–2002-05-31	4	2	SSMI/S (3), TMI, MHS (2)
PER01	1998-01-01–1999-12-31	4	0	SSMI/S (3), TMI
PER00	Before the 1998's	3	0	SSMI/S (3)
PER99	Before the 1991's	1	0	SSMI/S (1)

experiments hence provide sufficient samples to yield statistically sound results.

As previously mentioned, the series of data-denial experiments were designed and conducted based on distinct constellation configurations, which correspond to the period of satellite availability over the last few decades. In this case, a "golden era" satellite constellation, with 12 available passive microwave platforms, was found during the period from 2014 to 03-04 to 2015-04-08 (with the TRMM and GPM overlap period) and are adopted as a reference period (REF). Other seven homogeneous constellation configurations, with distinct platform types (i.e., number of available sounders and imagers), were identified between 1998- and 2017-years (PER01 for the oldest to PER07 to the most recent constellation period configuration). In addition, in order to investigate an extreme impact on the number of platforms to the overall precipitation uncertainty distributions, two other empirical configurations, which refer to period 1998, are considered: the so called "PER99", corresponding to the idealized case of a single SSM/I sensor, and the "PER00", aiming to simulate the impact of the group of SSM/I sensors (three platforms are considered) compared to a full constellation configuration. Fig. 5 and Table 1 summarize the adopted constellation configurations and their respective platforms and periods considered. As the rain-no rain detection step is deterministic, a single threshold of 0.5 mm h^{-1} for each platform is adopted for both the detection and intensity parameters. The analyses are carried out at the final daily accumulated precipitation over a quasi-global zone between 55° N/S, to benefit from the constellation of geostationary satellites. In order to exploit the seasonal impact on the daily precipitation uncertainties, the data-denial experiments were performed over two periods (JJA of 2014, DJF of 2014/5). Given that the same precipitation regime characteristics are considered and the associated uncertainties, consequently, would rely on the differences attributed to the group of satellites' changing (i.e., the impact of the constellation member in turn).

3.2. Comparison to the reference period

3.2.1. Satellite-satellite comparison

The distribution of uncertainty, here expressed as a relative difference between a period and the reference period, is very sensitive to the actual rainfall accumulation and to the configuration of the constellation (Fig. 6). Overall, the relative uncertainty can be as large as 200% in the low rain accumulation regimes, and decreases strongly with the rainfall amount. While PER99 is considered as an idealized worst-case scenario, it is also a good representation of single platform products (e.g., GPCP). The drastic differences shown here when compared to the full constellation demonstrates how strongly the uncertainty of daily rainfall can be impacted when different number of platforms are used (Chambon et al., 2013b). Beyond this extreme case, the relative uncertainty is not very large and is bounded within ~10%.

Overall, for each period, the uncertainty is slightly larger over ocean than over land at low-moderate precipitation amounts (<10 mm day^{-1}). On the other hand, at larger precipitation accumulations (e.g., > 50 mm day^{-1}), the uncertainties are larger over land than over ocean surfaces,

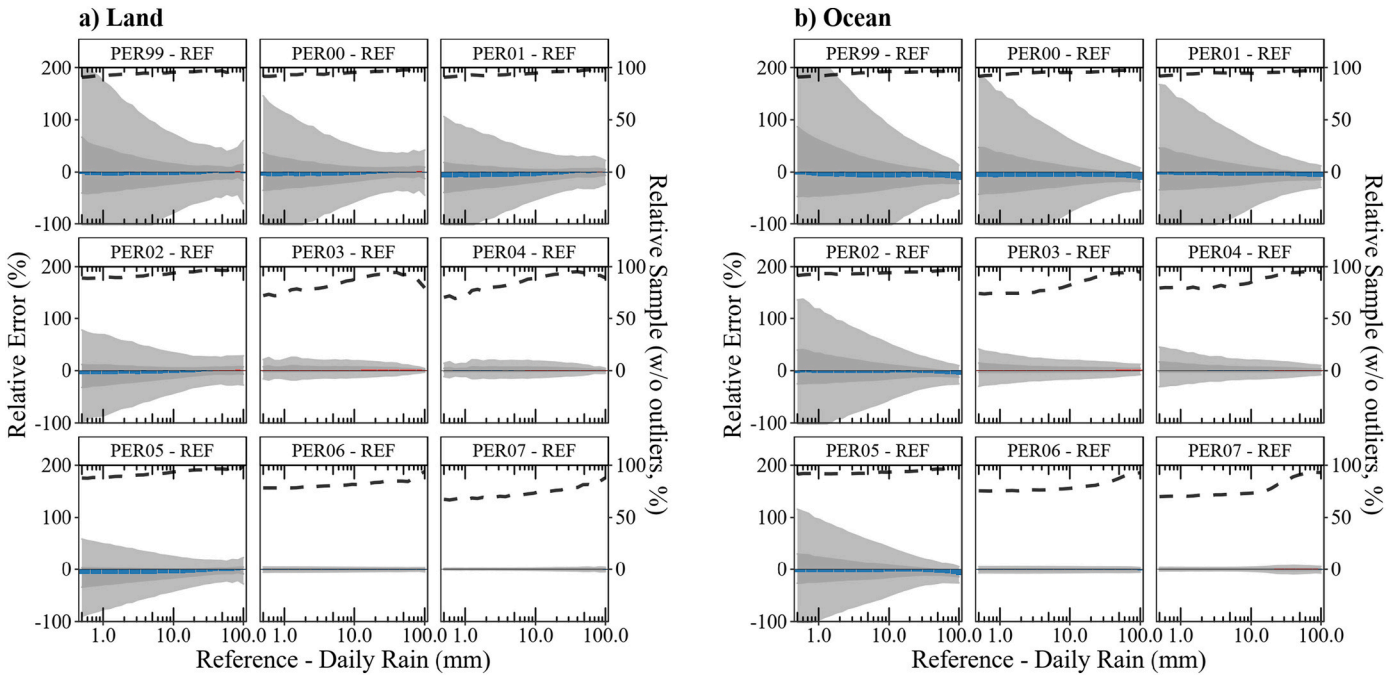

Fig. 6. The uncertainty distribution (left y-axis, in %) as a function of the rain (x-axis in log-scale, in mm), represented through the boxplot elements: the whiskers (25th/75th ± IQR*1.5, light gray shading), the IQR range (25th to 75th, dark gray shading) and the median (50th, in blue when negatively and in red when positively biased). The relative sample contribution of the actual sample (filtered out the outliers – within the range of 25th/75th ± IQR*1.5), related to the overall sample, are depicted by dashed lines on each panel (right y-axis, in %). The constellation-configuration experiments are compared to the "golden-era" constellation-period configuration as reference (REF), during JJA of 2014, over a) Land and b) Ocean surfaces and between 55°N/S global zones. (For interpretation of the references to colour in this figure legend, the reader is referred to the web version of this article.)

with a slight tendency to increase as precipitation accumulation increases. These land-ocean differences are attributed to the distinct precipitation regimes, driven by multiple precipitating systems and their extremes, which have considerable contributions of MCS's over tropical regions (Roca and Fiolleau, 2020). In fact, such characteristics can be evidenced according to the systematic artefact of sampling, which the satellite constellation configuration under consideration (i.e., the number and type of platform) impacts the quantification of the rainfall distribution over both the land and ocean surfaces globally differently. The uncertainty generally decreases with time, except for the PER05. PER05 is a short (~6 months) period in the first half of 2012 for which, both the AMSR-2 and AMSR-E imagers are absent – the AMSR-E (AQUA) imager reached it's 9+ year lifetime and was no longer available and the AMSR-2 imager on board GCOMW1 was not yet operational. Given that PER05 kept the same configuration as REF with respect to the sounders, the largest difference was on the imagers' sampling, due to the absence

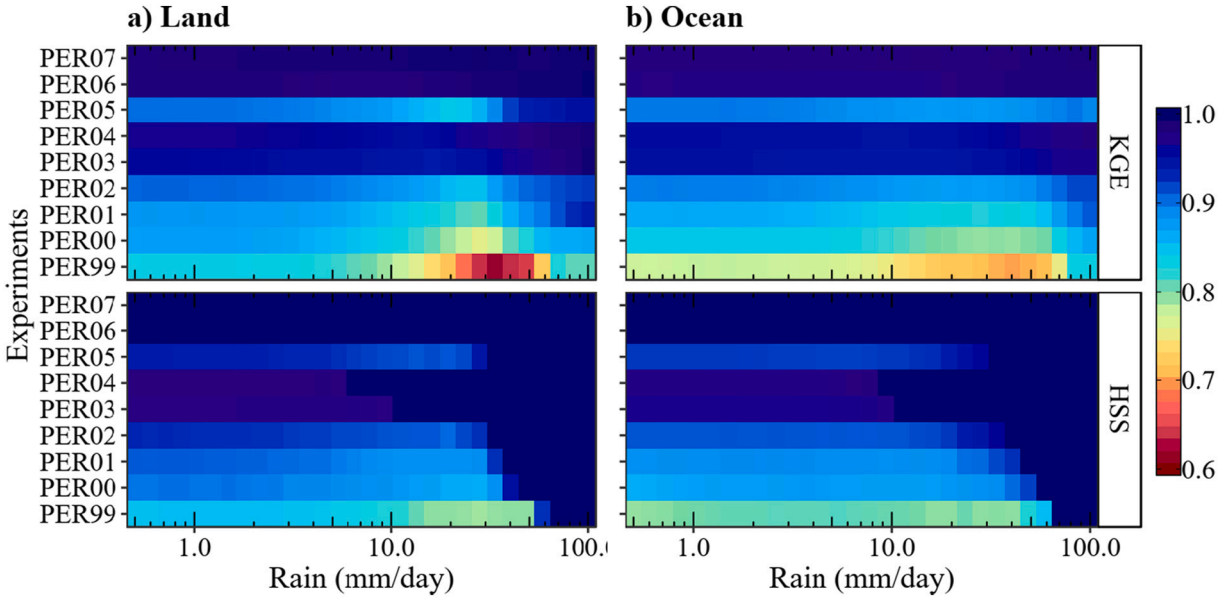

Fig. 7. Quasi-global (55° N/S) seasonal continuous (KGE, upper panels) and categorical (HSS, bottom panels) statistics for June–July-August of 2014, over a) Land and b) Ocean surface types, for each constellation period configuration experiment (y-axis), taking the "golden-era" constellation configuration as reference (REF). Note that the x-axis is in the log-scale.

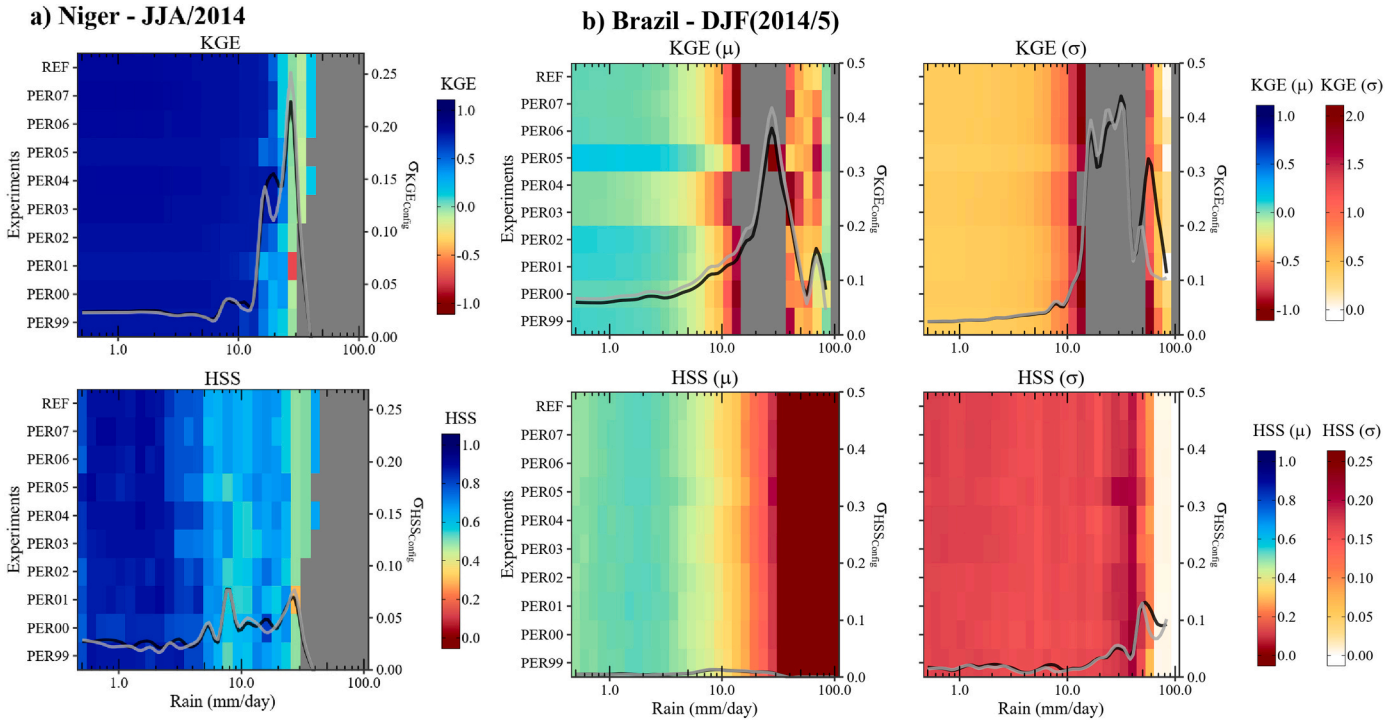

Fig. 8. Assessments of the constellation-period configurations using the ground-based precipitation as reference at a) Niger (JJA of 2014) and over b) Brazil (DJF of 2014/5). The intensity-scale statistical performances are summarized through the KGE (upper panels) and HSS (bottom panels) metrics. Over Brazil (regional scale), the statistical scores' distributions are represented by the mean (μ) and standard deviation (σ). The overall KGE and HSS variabilities, varying through the different constellation-period configurations – including (black solid line) and excluding (gray solid line) the PER99 and PER00 experiments, are depicted by the standard deviation (σConfig) on each log-binned rain intensity.

of both AMSR-2 and GMI imagers. As a result, PER05 uncertainty is larger than for the previous and following periods, with negative median bias over both the land and ocean surfaces along the entire rain range. The largest over-land (−ocean) negative median bias for PER05 was found at low-moderate (high, >50 mm day^{-1}) daily precipitation amounts, with about −15% (−12%). The over-land PER05 25th and 75th were about −30% and − 2%, respectively, whereas the over-ocean 25th and 75th were about −25% and 30% (spread of ~55%), respectively.

PER07 corresponds to the reference period minus TRMM/TMI and is shown to perform slightly less well than the reference, especially over the ocean, consistent with the estimated contribution of TRMM/TMI to tropical daily estimates (Roca et al., 2018). More quantitatively, when considering the 10 mm day^{-1} bin for instance, the spread in the differences over ocean as indicated with the 25th (75th) percentile, is larger by 15% (30%) than over land for the PER99 experiment. For PER07, the spread over land is small, with a value of the 25th (75th) percentile of −2.6% and + 0.7% and while the spread over the ocean remains small, it is larger by a factor of 2. The median of the distribution is mainly slightly negative and bounded by −8% and + 1.25%, for PER99 over ocean and PER03 over land, respectively.

Fig. 7 summarizes the constellation-period configurations' continuous and categorical statistical performances, through the Kling–Gupta Efficiency (KGE) and Heidke Skill Score (HSS) metrics, respectively (Gupta et al., 2009; Wilks, 2011; Kling et al., 2012). The land and ocean performance distributions are presented as a function of precipitation, for the period of JJA of 2014 and over a quasi-global (55° N/S) domain. The daily precipitation distributions, from each constellation configuration (PER99, PER00, …, PER07), are assessed via pixel-by-pixel comparison considering the 'golden era' configuration as a reference database (REF). In general, this analysis reveals how can the different constellation configurations modify the precipitation distribution, affecting the representation of both the detection and intensity of precipitation according to the surface type condition. Overall it is noted that the intensity-scale performances vary primarily according to the constellation configuration and, secondly to the surface type under consideration. The land/ocean differences were most evident in terms of intensity performance (KGE), even for high precipitation amounts. Further back in the constellation period, decreasing detection performance (HSS) is observed at high precipitation amounts. However, no impacts on precipitation detection were observed in any configuration greater than ~80 mm day^{-1}. Recent periods, especially the PER06 and PER07, followed by the PER03 and PER04, presented almost no impact, with both the KGE and HSS scores being very close to 1 (optimum skill score), regardless of both the precipitation threshold and the surface type conditions. Noteworthy, large precipitation systems are observed even with fewer samples, whereas small precipitating systems need better sampling to capture them properly and this can lead to large differences depending on the number and types of platform under consideration. On the other hand, the earlier configuration periods, including the PER05, has experienced larger KGE and HSS performance impacts, affecting the full precipitation range performances, especially seen at precipitation amounts from 10 to 60 mm day^{-1}, producing the lowest KGE values (between 0.6 and 0.7). The PER99 idealized case generated the lowest skill scores, underperforming where precipitation is between 20 and 50 mm day^{-1}, and more prominent over land with about 0.6 (~0.72 over ocean).

This suggests that the precipitation distribution, retrieved from the REF period, can be preserved even with the absence of certain platforms. In the meantime, it reveals the importance/predominance of certain platforms to the overall constellation configuration, which can lead to affect the performance distributions, especially the moderate-large precipitation amounts (10–50 mm day^{-1}), both in terms of detection and intensity. The modification of the constellation configuration, even considering an extreme situation (i.e., the PER99 case), did not show any impact on highest precipitation accumulations (e.g., >80 mm day^{-1}) in

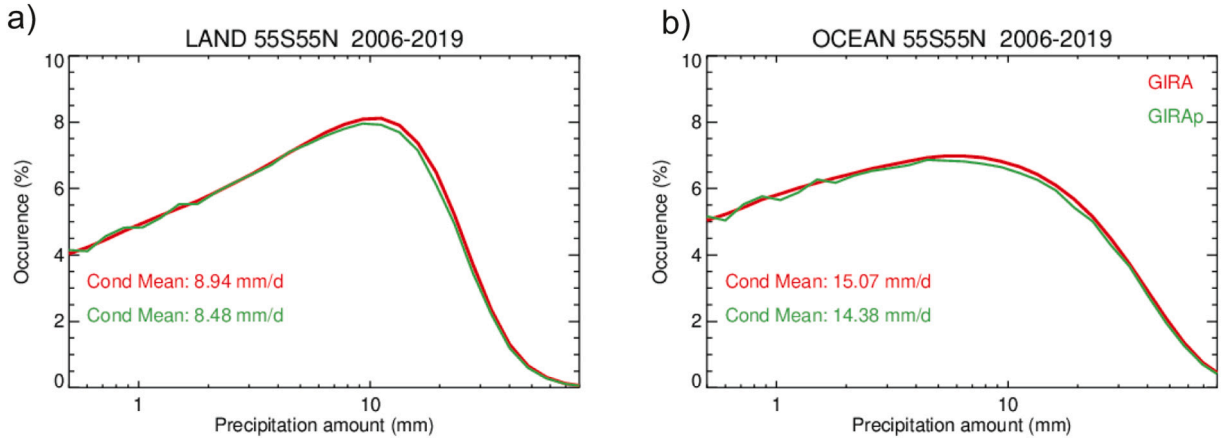

Fig. 9. Multi-year average distribution of occurrence as a function of the daily precipitation accumulation (probability density function) for GIRAFE (in red) and GIRAFE-corrected (in green), over a) land and b) ocean, for the 55°N/S global zone and during the period from 2006 to 2019. The correspondent daily precipitation conditional means are also indicated. (For interpretation of the references to colour in this figure legend, the reader is referred to the web version of this article.)

terms of detection, differently for the quantification performances. Hence, the performances can be attributed to distinct and joint assumptions, e.g., differences among the sensors, the retrieval 'ability', the number of samples, among others.

Finally, the experiment shows little to no sensitivity to the seasonality and the results are very similar when replicated for DJF instead of JJA (not shown).

3.2.2. Satellite and ground-based networks comparison

Fig. 8 summarizes, through the KGE and HSS skill scores, the performances of the constellation-period configurations with a focus on the two ground-based networks. Over Brazil, as the analyses were conducted for the whole country, the inter-pixel means μ and standard deviation σ were calculated for both KGE and HSS metrics. Additionally, the overall intensity-scale variabilities among all the constellation configurations σ_{Config} are also computed inclusive or not of the PER99 and PER00 experiments.

As shown in the satellite-satellite comparisons, the constellation configuration results in a slight impact on the overall intensity-scale performance distributions. The decay of both the continuous and categorical performances with the increase of daily rainfall intensity is seen regardless of constellation configuration. This is clearly observed at the local scale (over Niger), despite the sample limitations of large daily rain intensities (i.e., >20 mm day^{-1}), as well over Brazil, which has stronger regional variability signals, especially around 15–35 mm day^{-1}. The ability to quantify and detect moderate to high rainfalls, for instance around the 15–35 mm day^{-1} thresholds, are negatively skewed, seen both locally (Fig. 8a) and regionally (characterized by lower μ and higher σ values, Fig. 8b). Over Brazil, the largest regional uncertainty contrasts, were found in quantitative terms, i.e., KGE σ ranging from 0.2 to 2.0. The minimum (maximum) peaks of KGE μ (σ) were mostly concentrated around 15–35 mm day^{-1} (15–50 mm day^{-1}), including the PER99. Qualitatively, the minimum (maximum) values of HSS μ (σ), lower (greater) than 0.2, were observed at precipitation thresholds >30 mm day^{-1}, except above 60 mm day^{-1}, which presented the lowest HSS σ (between 0.05 and 0.15) among all precipitation classes and all the constellation configurations.

Therefore, these overall local and regional characteristics leaded to the largest skill variations among all the constellation configurations (σ_{Config}), that were mostly evident through the KGE and specially for precipitation intensities >10 mm day^{-1}. Below this threshold of ~10 mm day^{-1}, no considerable σ_{Config} differences, between with and without the PER99 and PER00, were encountered through both KGE and HSS. Over Niger, the highest KGE σ_{Config} (~0.25) was observed at precipitation intensities roughly 25 mm day^{-1}, where the differences of whether or not considering the PER99 and PER00 were slightly higher compared to other precipitation classes. These σ_{Config} KGE and HSS results on the local scale are confirmed regionally. The largest KGE σ_{Config} around 25 mm day^{-1}, demonstrated through both KGE μ and σ, was observed whether or not considering the PER99 and PER00 experiments. In fact, the largest KGE skill variability differences were mainly encountered at precipitation >50 mm day^{-1}, where the PER99 and PER00 experiments contribute to increase the variability with about 0.33 of $\sigma_{KGEConfig}$ (~0.2 without the PER99 and PER00). Through the categorical verification, almost no differences in the σ_{Config} were found on HSS σ. For precipitation intensities above 50 mm day^{-1}, the highest σ peaks between 0.15 and 0.19 were found, whereas other categories of precipitation experienced HSS σ values below 0.025. Thus, the detection, was found to be less sensitive to the constellation configuration modification according to the intensity-scale performance, despite older configurations having decreased ability to detect events above 30 mm day^{-1}, versus 50 mm day^{-1} for more recent configurations (clearly noted at local scale). Regionally, the differences among the constellation configurations are negligible, although at higher accumulations the signs of performance variability are clearer.

4. Application to the GIRAFE 2006–2019 record

4.1. Approximation of the uncertainty distribution

In order to make use of these uncertainty distribution and instead of using these differences as look-up tables, the distributions have been successfully summarized by fitting with a Gaussian Mixture Model (GMM, Lerch et al., 2020). The details of the implementation of the fitting model and its evaluation are presented in a companion paper (Oliveira and Roca, 2022). The coefficients of the GMM have been fitted separately over land and over ocean for each of the listed periods. These approximate GMMs are then used for bootstrapping computations as discussed below.

4.2. Time-dependent uncertainty bootstrapping

The results of the previous section are now put back into a physical time line. For each JJA season from 2006 to 2019, the relevant period is first identified thanks to Fig. 5 data. The corresponding GMM coefficients are used to simulate the GIRAFE histogram that would account for the constellation change. For each day of JJA for each year, for each grid point, 1000 random samples are taken from the GMM uncertainty model. The anomaly is added to the actual grid point value and a "bootstrapped" histogram is built. The procedure is repeated for each

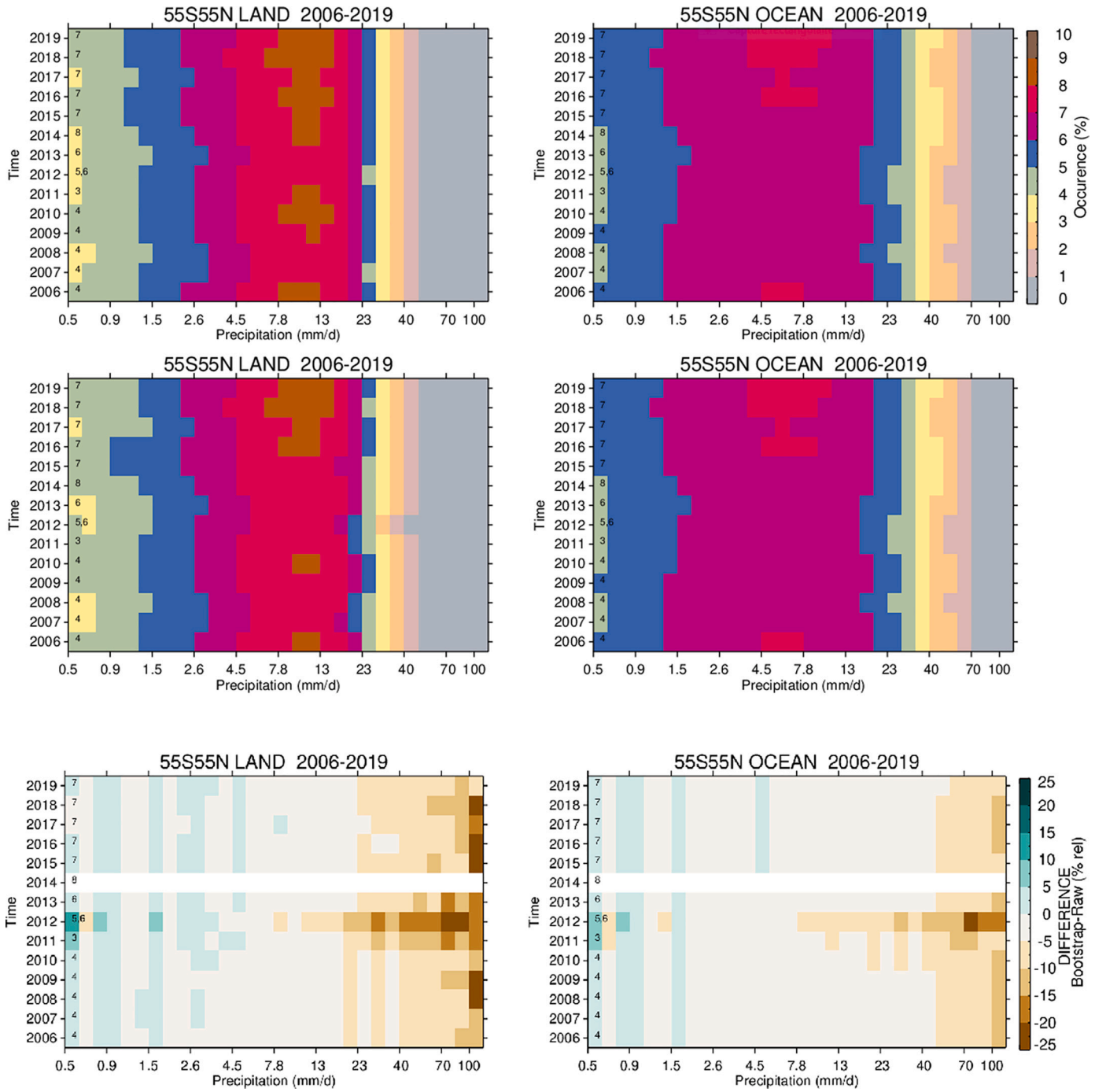

Fig. 10. Time evolution of the occurrence distribution as a function of the daily rainfall accumulation. For 55°s-55°n land (left) and ocean (right). For GIRAFE (top) and GIRAFE corrected (top-middle). Relative difference (bottom). The true zero of the differences are shown in white. Small digits at the lower end of the spectrum indicate the corresponding period identifier for each year.

day of the season. The final histogram is divided by 1000 to ensure consistency with the raw dataset. Ocean and land are processed separately to account for the previously highlighted differences in the impact of the constellation change. Results below do not show a strong sensitivity to the number of simulations as long as the sampling is greater than ~200.

4.3. Long term average and interannual variability

For long term averages, the impact of changes in the constellation over time are negligible. Multi-year conditional average precipitation over both land and ocean varies by less of 5% when the change in constellation is accounted for. Similarly, the multi-year average distribution of occurrence exhibits a very small sensitivity to the changes of configuration of the constellation (Fig. 9).

Fig. 10 shows the time series of the annual histogram of daily precipitation for the raw GIRAFE record and the bootstrapped one for land and ocean over the 2006–2020 period. Again, the differences seem small. Yet, the analysis reveals a dependency of the difference in the rain accumulation intensity. In agreement with the results presented in the previous sections, the large accumulation (>40 mm day^{-1}) are affected relatively more than the other part of the distribution, more so over land

than over ocean. As expected the periods after 2012 (PER06 and PER07) are very close to the reference PER08 (in 2014) and as not associated with strong correction (See Section 3). On the other hand, the period before 2012, corresponding to PER03, departs more from the reference and consequently is associated with a stronger impact on the distribution. In 2012, the summer is split into PER06 and period PER05, associated with a strong departure from the reference, that explain the stronger correction observed for this year over land. Prior to the 2010 epoch, the large rain accumulations are mainly impacted with amounts larger than 70 mm day^{-1} being 5–10% less frequent over the ocean, once the constellation change is accounted for (Fig. 10 bottom-right).

Over the ocean, the time series of the GIRAFE histogram indicates an anomalous year in 2012 with a greater skewed distribution compared to the other years that corresponds to PER05 and PER06. This is also seen in GIRAFE-Bootstrapped (Fig. 10) suggesting that this feature is not an artefact from changes in the constellation. It is also interesting to note that in 2009, the replacement of one SSM/I instrument by a newer SSM/IS instrument does not seem to impact the constellation based product, unlike it does for single platform product (Potter et al., 2020).

5. Conclusions

A prototype version of a climate-oriented global precipitation algorithm is used to explore the impact of the changing passive microwave constellation configuration on the precipitation estimate. The experimental product exhibits the well-known precipitation climatological features and compares well with a limited validation dataset, but for the very high daily accumulation that do not show as good performances as for the moderate accumulation. Data denial experiments are performed to mimic the evolution of the passive microwave constellation configuration over the last decades. The resulting differences are analyzed with respect to a reference period that correspond to the most populated constellation (in 2014). The differences are shown to depend on the period and the number of platforms available as well as on the rain accumulation. To a lesser extent, the uncertainty is slightly larger over ocean than over land. Also, the more the period under consideration is different from the reference period, the larger the differences. The distribution of uncertainty per period is used in the time chronology to rebuild a corrected time series of the product that account for the changes in time of the constellation configuration. The results indicate a negligible impact for long term global average and a significant (>10%) impact on the interannual variability, mainly over land and for accumulation >25 mm day^{-1}. The approach presented here is very generic and while illustrated using the GIRAFE framework, it is likely to be representative of various precipitation CDRs built using the GPM constellation.

Future work will be directed to source of uncertainty compared to other source of uncertainties for climate trends analysis. The operational GIRAFE product will have a global coverage and further work is required to assess how the regions poleward of 55° are impacted with emphasis on the latitudinal sampling from the precessing missions (e.g., TRMM, Megha-Tropiques and GPM). Generally, regional investigation would also be a way to analyze the sensitivity of specific-rainfall regimes to the configuration of the constellation but the adequation of the duration of the data denial experiments would need to be reassessed for that endeavor.

While this study is focused on precipitation, the methodology and rationale developed here should be also useful for improving CDRs for other ECVs that also depend on a suite of platforms, if not a constellation, such as SST (Donlon et al., 2012) or cloud climatology (Karlsson et al., 2017). To a large extent, such an effort could in principle also guide the assessment of reanalysis that suffers from the same time-dependent amount of assimilated data (Hersbach et al., 2020).

Authors statements

All authors edited the manuscript and perform the reviewing

CRediT authorship contribution statement

Rômulo Augusto Jucá Oliveira: Conceptualization, Writing – original draft. **Rémy Roca:** Conceptualization, Writing – original draft. **Stephan Finkensieper:** Data curation, Writing – original draft. **Sophie Cloché:** Data curation. **Marc Schröder:** Conceptualization.

Declaration of Competing Interest

The authors declare that they have no known competing financial interests or personal relationships that could have appeared to influence the work reported in this paper.

Data availability

Data will be made available on request.

Acknowledgements

We thank M. Gosset and T. Fiolleau for interesting discussions on tropical precipitation and satellite observations. We also thank T. Sikorski for his help with Fig. 1. The authors also extend their gratitude to D. Vila for his support in accessing the Brazilian ground observations. We thank the anonymous reviewers for their many insightful comments and suggestions, which improved the clarity and quality of the manuscript. This study benefited from the IPSL mesocenter ESPRI facility which is supported by CNRS, Sorbonne Université, UVSQ, CNES, Ecole Polytechnique and national research infrastructures Climeri-France and DATA TERRA. This study was performed by the EUMETSAT Satellite Application Facility on Climate Monitoring, and we acknowledge the financial support by the EUMETSAT member states through CM SAF.

References

Adler, R.F., et al., 2018. The Global Precipitation Climatology Project (GPCP) monthly analysis (New Version 2.3) and a review of 2017 global precipitation. Atmosphere (Basel). 9 https://doi.org/10.3390/atmos9040138.

Alexander, L.V., Bador, M., Roca, R., Contractor, S., Donat, M.G., Nguyen, P.L., 2020. Intercomparison of annual precipitation indices and extremes over global land areas from in situ, space-based and reanalysis products. Environ. Res. Lett. 15 https://doi.org/10.1088/1748-9326/ab79e2.

AMMA-CATCH, 1990. AMMA-CATCH: a hydrological, meteorological and ecological observatory on West Africa. In: IRD, CNRS-INSU, OSUG, OMP, OREME. https://doi.org/10.17178/AMMA-CATCH.all.

AMMA-CATCH Niger, 1990. AMMA-CATCH observatory: Niamey square degree mesoscale site (16 000 km2) in the cultivated Sahelian zone, Niger. https://doi.org/10.17178/AMMA-CATCH.niger.

Ayat, H., Evans, J.P., Behrangi, A., 2021. How do different sensors impact IMERG precipitation estimates during hurricane days? Remote Sens. Environ. 259, 112417 https://doi.org/10.1016/j.rse.2021.112417.

Bador, M., Alexander, L.V., Contractor, S., Roca, R., 2020. Diverse estimates of annual maxima daily precipitation in 22 state-of-the-art quasi-global land observation datasets. Environ. Res. Lett. https://doi.org/10.1088/1748-9326/ab6a22.

Beck, H.E., et al., 2017. Global-scale evaluation of 22 precipitation datasets using gauge observations and hydrological modeling. Hydrol. Earth Syst. Sci. 21, 6201–6217. https://doi.org/10.5194/hess-21-6201-2017.

Biscaro, T.S., Machado, L.A.T., Giangrande, S.E., Jensen, M.P., 2021. What drives daily precipitation over the Central Amazon? Differences observed between wet and dry seasons. Atmos. Chem. Phys. 21, 6735–6754. https://doi.org/10.5194/acp-21-6735-2021.

Cai, W., et al., 2020. Climate impacts of the El Niño–Southern Oscillation on South America. Nat. Rev. Earth Environ. 1, 215–231. https://doi.org/10.1038/s43017-020-0040-3.

Chambon, P., Jobard, I., Roca, R., Viltard, N., 2012. An investigation of the error budget of tropical rainfall accumulation derived from merged passive microwave and infrared satellite measurements. Q. J. R. Meteorol. Soc. 139, 879–893. https://doi.org/10.1002/qj.1907.

Chambon, P., Jobard, I., Roca, R., Jobard, I., Capderou, M., 2013a. The sensitivity of tropical rainfall estimation from satellite to the configuration of the microwave

imager constellation. IEEE Geosci. Remote Sens. Lett. 10, 996–1000. https://doi.org/10.1109/LGRS.2012.2227668.
Chambon, P., Jobard, I., Roca, R., Jobard, I., Capderou, M., 2013b. The Sensitivity of Tropical Rainfall Estimation from Satellite to the Configuration of the Microwave Imager Constellation. IEEE Geosci. Remote Sens. Lett. 10, 996–1000. https://doi.org/10.1109/lgrs.2012.2227668.
Chen, G., Norris, J., David Neelin, J., Lu, J., Ruby Leung, L., Sakaguchi, K., 2019. Thermodynamic and dynamic mechanisms for hydrological cycle intensification over the full probability distribution of precipitation events. J. Atmos. Sci. 76, 497–516. https://doi.org/10.1175/JAS-D-18-0067.1.
Coelho, C.A.S., Cardoso, D.H.F., Firpo, M.A.F., 2016. Precipitation diagnostics of an exceptionally dry event in São Paulo, Brazil. Theor. Appl. Climatol. 125, 769–784. https://doi.org/10.1007/s00704-015-1540-9.
Contractor, S., Donat, M.G., Alexander, L.V., 2021. Changes in observed daily precipitation over global land areas since 1950. J. Clim. 34, 3–19. https://doi.org/10.1175/JCLI-D-19-0965.1.
Costa, I.C., Machado, L.A.T., Kummerow, C., 2018. An examination of microwave rainfall retrieval biases and their characteristics over the Amazon. Atmos. Res. 213, 323–330. https://doi.org/10.1016/j.atmosres.2018.06.011.
Donlon, C.J., Martin, M., Stark, J., Roberts-Jones, J., Fiedler, E., Wimmer, W., 2012. The Operational Sea Surface Temperature and Sea Ice Analysis (OSTIA) system. Remote Sens. Environ. 116, 140–158. https://doi.org/10.1016/j.rse.2010.10.017.
Fiolleau, T., Roca, R., Cloche, S., Bouniol, D., Raberanto, P., 2020. Homogenization of geostationary infrared imager channels for cold cloud studies using megha-tropiques/ScaRaB. IEEE Trans. Geosci. Remote Sens. 1–14 https://doi.org/10.1109/tgrs.2020.2978171.
Gosset, M., Alcoba, M., Roca, R., Cloché, S., Urbani, G., 2018. Evaluation of TAPEER daily estimates and other GPM-era products against dense gauge networks in West Africa, analysing ground reference uncertainty. Q. J. R. Meteorol. Soc. 144, 255–269. https://doi.org/10.1002/qj.3335.
Gupta, H.V., Kling, H., Yilmaz, K.K., Martinez, G.F., 2009. Decomposition of the mean squared error and NSE performance criteria: Implications for improving hydrological modelling. J. Hydrol. 377, 80–91. https://doi.org/10.1016/j.jhydrol.2009.08.003.
Hersbach, H., et al., 2020. The ERA5 global reanalysis. Q. J. R. Meteorol. Soc. 1999–2049 https://doi.org/10.1002/qj.3803.
Huffman, G.J., et al., 2001. Global precipitation at one-degree daily resolution from multisatellite observations. J. Hydrometeorol. 2, 36–50. https://doi.org/10.1175/1525-7541(2001)002<0036:GPAODD>2.0.CO;2.
Huffman, G.J., et al., 2018. Algorithm Theoretical Basis Document (ATBD) NASA Global Precipitation Measurement (GPM) Integrated Multi-satellitE Retrievals for GPM (IMERG) Prepared by.
Joyce, R.J., Janowiak, J.E., Arkin, P.A., Xie, P., 2004. CMORPH: a Method that Produces Global Precipitation estimates from Passive Microwave and infrared Data at High Spatial and Temporal Resolution. J. Hydrometeorol. 5, 487–503. https://doi.org/10.1175/1525-7541(2004)005<0487:CAMTPG>2.0.CO;2.
Karlsson, K.G., et al., 2017. CLARA-A2: the second edition of the CM SAF cloud and radiation data record from 34 years of global AVHRR data. Atmos. Chem. Phys. 17, 5809–5828. https://doi.org/10.5194/acp-17-5809-2017.
Kidd, C., Kniveton, D.R., Todd, M.C., Bellerby, T.J., 2003. Satellite rainfall estimation using combined passive microwave and infrared algorithms. J. Hydrometeorol. 4, 1088–1104. https://doi.org/10.1175/1525-7541(2003)004<1088:sreucp>2.0.co;2.
Kidd, C., Kniveton, D.R., Huffman, G., Maggioni, V., Chambon, P., Oki, R., 2021a. The global satellite precipitation constellation: current status and future requirements. Bull. Am. Meteorol. Soc. 1–47 https://doi.org/10.1175/bams-d-20-0299.1.
Kidd, C., Kniveton, D.R., Matsui, T., Ringerud, S., 2021b. Precipitation retrievals from passive microwave cross-track sensors: the precipitation retrieval and profiling scheme. Remote Sens. 13, 1–15. https://doi.org/10.3390/rs13050947.
Kirstetter, P.-E., Viltard, N., Gosset, M., 2013. An error model for instantaneous satellite rainfall estimates: evaluation of BRAIN-TMI over West Africa. Q. J. R. Meteorol. Soc. 139, 894–911.
Kling, H., Fuchs, M., Paulin, M., 2012. Runoff conditions in the upper Danube basin under an ensemble of climate change scenarios. J. Hydrol. 424–425, 264–277. https://doi.org/10.1016/j.jhydrol.2012.01.011.
Kummerow, C., Olson, W.S., Giglio, L., 1996. A simplified scheme for obtaining precipitation and vertical hydrometeor profiles from passive microwave sensors. IEEE Trans. Geosci. Remote Sens. 34, 1213–1232. https://doi.org/10.1109/36.536538.
Kummerow, C.D., Randel, D.L., Kulie, M., Wang, N.Y., Ferraro, R., Joseph Munchak, S., Petkovic, V., 2015. The evolution of the Goddard profiling algorithm to a fully parametric scheme. J. Atmos. Ocean. Technol. 32, 2265–2280. https://doi.org/10.1175/JTECH-D-15-0039.1.
Lerch, F., Ultsch, A., Lotsch, J., 2020. Distribution Optimization: an evolutionary algorithm to separate Gaussian mixtures. Sci. Rep. 10, 648. https://doi.org/10.1038/s41598-020-57432-w.
Levizzani, V., Cattani, E., 2019. Satellite Remote Sensing of Precipitation and the Terrestrial Water Cycle in a changing climate. Remote Sens. 11, 2301. https://doi.org/10.3390/rs11192301.
Levizzani, V., et al., 2018. The activities of the International Precipitation Working Group. Q. J. R. Meteorol. Soc. https://doi.org/10.1002/qj.3214.
Liu, C., Allan, R.P., 2012. Multisatellite observed responses of precipitation and its extremes to interannual climate variability. J. Geophys. Res. Atmos. 117, 1–16. https://doi.org/10.1029/2011JD016568.
Maggioni, V., Meyers, P.C., Robinson, M.D., 2016. A Review of Merged High-Resolution Satellite Precipitation Product Accuracy during the Tropical Rainfall measuring Mission (TRMM) era. J. Hydrometeorol. 17, 1101–1117. https://doi.org/10.1175/JHM-D-15-0190.1.
Marengo, J.A., et al., 2012. Recent developments on the south American monsoon system. Int. J. Climatol. 32, 1–21. https://doi.org/10.1002/joc.2254.
Marengo, J.A., Fisch, G.F., Alves, L.M., Sousa, N.V., Fu, R., Zhuang, Y., 2017. Meteorological context of the onset and end of the rainy season in Central Amazonia during the GoAmazon2014/5. Atmos. Chem. Phys. 17, 7671–7681. https://doi.org/10.5194/acp-17-7671-2017.
Masunaga, H., Schröder, M., Furuzawa, F.A., Kummerow, C., Rustemeier, E., Schneider, U., 2019. Inter-product biases in global precipitation extremes. Environ. Res. Lett. 14, 125016 https://doi.org/10.1088/1748-9326/ab5da9.
Morin, E., 2011. To Know What We Cannot Know: Global Mapping of Minimal, 47, pp. 1–9. https://doi.org/10.1029/2010WR009798.
Oliveira, R.A.J., Roca, R., 2022. A simple statistical model of the uncertainty distribution for daily gridded precipitation multi-platform satellite products. 2022. Remote Sens. 14 (15), 3726. https://doi.org/10.3390/rs14153726.
Oliveira, R., Maggioni, V., Vila, D., Morales, C., 2016. Characteristics and diurnal cycle of GPM rainfall estimates over the Central Amazon region. Remote Sens. 8 https://doi.org/10.3390/rs8070544.
Pendergrass, A.G., Hartmann, D.L., 2014a. Changes in the distribution of rain frequency and intensity in response to global warming. J. Clim. 27, 8372–8383. https://doi.org/10.1175/JCLI-D-14-00183.1.
Pendergrass, A.G., Hartmann, D.L., 2014b. Two modes of change of the distribution of rain. J. Clim. 27, 8357–8371. https://doi.org/10.1175/JCLI-D-14-00182.1.
Petković, V., Kummerow, C.D., 2017. Understanding the sources of satellite passive microwave rainfall retrieval systematic errors over land. J. Appl. Meteorol. Climatol. 56, 597–614. https://doi.org/10.1175/JAMC-D-16-0174.1.
Potter, G.L., Huffman, G.J., Bolvin, D.T., Bosilovich, M.G., Hertz, J., Carriere, L.E., 2020. Histogram anomaly time series : a compact graphical representation of spatial time series data sets. Bull. Am. Meteorol. Soc. 101, E2133–E2137. https://doi.org/10.1175/BAMS-D-20-0130.1.
Raia, A., Cavalcanti, I.F.A., 2008. The Life Cycle of the South American Monsoon System. J. Clim. 21, 6227–6246. https://doi.org/10.1175/2008JCLI2249.1.
Rajagopal, M., Zipser, E., Huffman, G., Russell, J., Tan, J., 2021. Comparisons of IMERG version 06 precipitation at and between passive microwave overpasses in the tropics. J. Hydrometeorol. 22, 2117–2130. https://doi.org/10.1175/JHM-D-20-0226.1.
Raspaud, M., et al., 2021. pytroll/satpy: Version 0.29.0. https://doi.org/10.5281/ZENODO.4904606.
Reboita, M.S., Gan, M.A., da Rocha, R.P., Ambrizzi, T., 2010. Regimes de precipitação na América do Sul: uma revisão bibliográfica. Rev. Bras. Meteorol. 25, 185–204. https://doi.org/10.1590/s0102-77862010000200004.
Roca, R., Fiolleau, T., 2020. Extreme precipitation in the tropics is closely associated with long-lived convective systems. Commun. Earth Environ. 1, 1–6. https://doi.org/10.1038/s43247-020-00015-4.
Roca, R., Chambon, P., Jobard, I., Kirstetter, P.E., Gosset, M., Bergés, J.C., 2010. Comparing satellite and surface rainfall products over West Africa at meteorologically relevant scales during the AMMA campaign using error estimates. J. Appl. Meteorol. Climatol. 49, 715–731. https://doi.org/10.1175/2009JAMC2318.1.
Roca, R., et al., 2015. The Megha-Tropiques mission: a review after three years in orbit. Front. Earth Sci. 3, 17.
Roca, R., et al., 2018. Quantifying the Contribution of the Megha-Tropiques Mission to the Estimation of Daily Accumulated Rainfall in the Tropics, 144, pp. 49–63. https://doi.org/10.1002/qj.3327.
Roca, R., Alexander, L.V., Potter, G., Bador, M., Jucá, R., Contractor, S., Bosilovich, M.G., Cloché, S., 2019. FROGS: a daily $1^\circ \times 1^\circ$ gridded precipitation database of rain gauge, satellite and reanalysis products. Earth Syst. Sci. Data 11, 1017–1035. https://doi.org/10.5194/essd-11-1017-2019.
Roca, R., Guérou, A., Oliveira, R.A. Jucá, Chambon, P., Gosset, M., Cloché, S., Schröder, M., 2020. Merging the infrared fleet and the microwave constellation for tropical hydrometeorology (TAPEER) and global climate monitoring (GIRAFE) applications. Adv. Global Change Res. 67 of, 429–450.
Roca, R., et al., 2021. The Joint IPWG/GEWEX Precipitation Assessment. R. Roca and Z. S. Haddad, Eds. World Climate Research Programme, p. 125.
Stephens, G.L., Slingo, J.M., Rignot, E., Reager, J.T., Hakuba, M.Z., Durack, P.J., Worden, J., Rocca, R., 2020. Earth's water reservoirs in a changing climate. Proc. R. Soc. A Math. Phys. Eng. Sci. 476 https://doi.org/10.1098/rspa.2019.0458.
Sun, Q., Miao, C., Duan, Q., Ashouri, H., Sorooshian, S., Hsu, K.L., 2018. A review of global precipitation data sets: data sources, estimation, and intercomparisons. Rev. Geophys. 56, 79–107. https://doi.org/10.1002/2017RG000574.
Szantai, A., Six, B., Cloché, S., Sèze, G., 2011. Quality of geostationary satellite images. In: Megha-Tropiques Tech. Memo, p. 3.
Tan, J., Petersen, W.A., Kirchengast, G., Goodrich, D.C., Wolff, D.B., 2018. Evaluation of global precipitation measurement rainfall estimates against three dense gauge networks. J. Hydrometeorol. 19, 517–532. https://doi.org/10.1175/JHM-D-17-0174.1.
Utsumi, N., Turk, F.J., Haddad, Z.S., Kirstetter, P.E., Kim, H., 2020. Evaluation of precipitation vertical profiles estimated by GPM-Era satellite-based passive microwave retrievals. J. Hydrometeorol. 22, 95–112. https://doi.org/10.1175/JHM-D-20-0160.1.
Wilks, D.S., 2011. Statistical Methods in the Atmospheric Sciences. Academic Press, p. 704.
Xu, L., Gao, X., Sorooshian, S., Arkin, P.A., Imam, B., 1999. A microwave infrared threshold technique to improve the GOES precipitation index. J. Appl. Meteorol. 38, 569–579. https://doi.org/10.1175/1520-0450(1999)038<0569:AMITTT>2.0.CO;2.
You, Y., Petkovic, V., Tan, J., Kroodsma, R., Berg, W., Kidd, C., Peters-Lidard, C., 2020. Evaluation of v05 precipitation estimates from gpm constellation radiometers using

kupr as the reference. J. Hydrometeorol. 21, 705–728. https://doi.org/10.1175/JHM-D-19-0144.1.